Journal of Magnetic Resonance **152,** 189–194 (2001)
doi:10.1006/jmre.2001.2391, available online at http://www.idealibrary.com on IDEAL®

COMMUNICATION

MR Imaging with Phase Encoding of Intermolecular Multiple Quantum Coherences

S. Sendhil Velan, P. T. Narasimhan, and Russell E. Jacobs[1]

Biological Imaging Center, 139-74 Beckman Institute, California Institute of Technology, Pasadena, California 91125

Received March 7, 2001; revised June 8, 2001

Novel 2D and 3D pulse sequences producing images through the phase encoding of intermolecular multiple quantum coherences (i-MQCs) are presented. The signal acquired with these sequences is free from intermolecular zero quantum coherences (i-ZQCs) which are not phase encoded and additional phase cycling eliminates artifacts. Phase encoding during the *n*-quantum evolution period provides *n* times the resolution expected from equivalent phase encoding of the reconverted single quantum coherences. These sequences have potential applications for producing i-MQC images of biological tissues as well as nonbiological materials with substantial amounts of water. © 2001 Academic Press

Key Words: **MR imaging; intermolecular multiple quantum coherences; i-MQC phase encoding; resolution.**

Intermolecular multiple quantum coherences (i-MQCs) created from the distant dipolar field have been employed for producing magnetic resonance images (*1–8*). The imaging sequences are based on the CRAZED (*9*) (COSY Revamped by Asymmetric Z-Gradient Echo Detection) sequence for creating i-MQCs and the HOMOGENIZED (*10*) (HOMOGeneity ENhancement by Intermolecular ZEro Quantum Detection) sequence for creating intermolecular zero quantum coherences (i-ZQCs). In the past, the technique of phase encoding multiple quantum coherences has been carried out only in systems with intramolecular coupled spins (*11–13*). The creation of i-MQCs, however, does not demand the presence of intramolecular spin couplings and can thus be applied in a wide range of systems including biological specimens.

Sequences for the creation of i-MQCs (*1–8*) usually apply a RF pulse followed by a gradient pulse that modulates the transverse magnetization into a helical structure. The pitch length, p, of the helix is given by $2\pi/\gamma Gt$ where γ is the gyromagnetic ratio, G is the gradient strength, and t is the duration of the gradient. The signal is generated from pairs of spins within a correlation distance $d = \pi/\gamma Gt$ that is half the repeat distance of the helix (*1*). The ability to potentially manipulate image contrast by changing the helix pitch and thus altering the interaction distance between the spins makes this technique of interest for biological and clinical imaging. Previous work employing i-MQCs to produce MR images adopted multiple quantum filtering strategies that convert i-MQCs to single quantum coherences that are then phase and frequency encoded (*1–8*). In this Communication, we demonstrate a novel approach for creating i-MQC images of water protons with enhanced resolution by phase encoding the i-MQCs during their evolution.

Figure 1 displays the pulse sequence used to produce 2D slice-selective images employing i-MQCs. The first 90° pulse creates i-MQCs and i-ZQCs. The coherence gradient G_1, on during the i-MQC evolution period, creates a magnetization helix with pitch length of $2\pi/\gamma G_1 t$. The phase-encoding gradient G_p is also on during the evolution period of the i-MQCs. The i-ZQCs are insensitive to gradients and are thus not phase encoded. However, in the case of $k = 0$ one might expect contributions from i-ZQCs. Such contributions can be suppressed by employing appropriate phase-cycling schemes. The second pulse ($\theta°$) is issued at the optimum flip angle for maximizing reconversion of i-MQCs into SQCs. For intermolecular double quantum coherences (i-DQCs) the optimum angle is 120 or 60° depending on echo or antiecho selection. $\theta = 90°$ can be employed for reconversion of other higher order i-MQCs. The period between the first 90° pulse and the $\theta°$ reconversion pulse, τ_{iMQ}, can be varied to produce contrast that depends on the transverse relaxation of i-MQCs ($T_2^{*,\text{i-MQC}}$). The coherence selection gradient G_2 of amplitude nG_1 unwinds the helix. The period after reconversion, $\Delta + \text{TE}/2$, is optimized to produce coherence transfer echoes of coherence order n (*14*). Depending on the relative gradient polarity of the coherence transfer selection gradient pair G_1 and G_2, coherence transfer echoes or anti echoes can be generated. The coherence gradient G_1 can be placed anywhere between the first 90° pulse and the $\theta°$ reconversion pulse (*15*). The final 180° pulse is a slice-selective-shaped pulse. G_{Slice} is the slice-selective gradient and the pair $G_{\text{Cr}'}$ symmetric to the slice-selective gradient are crushers. G_{RBal} is the read compensation gradient

[1] To whom correspondence should be addressed at 139-74 Beckman Institute, Caltech, Pasadena, CA 91125. Fax: (626) 449-5163. E-mail: rjacobs@caltech.edu.

1090-7807/01 $35.00

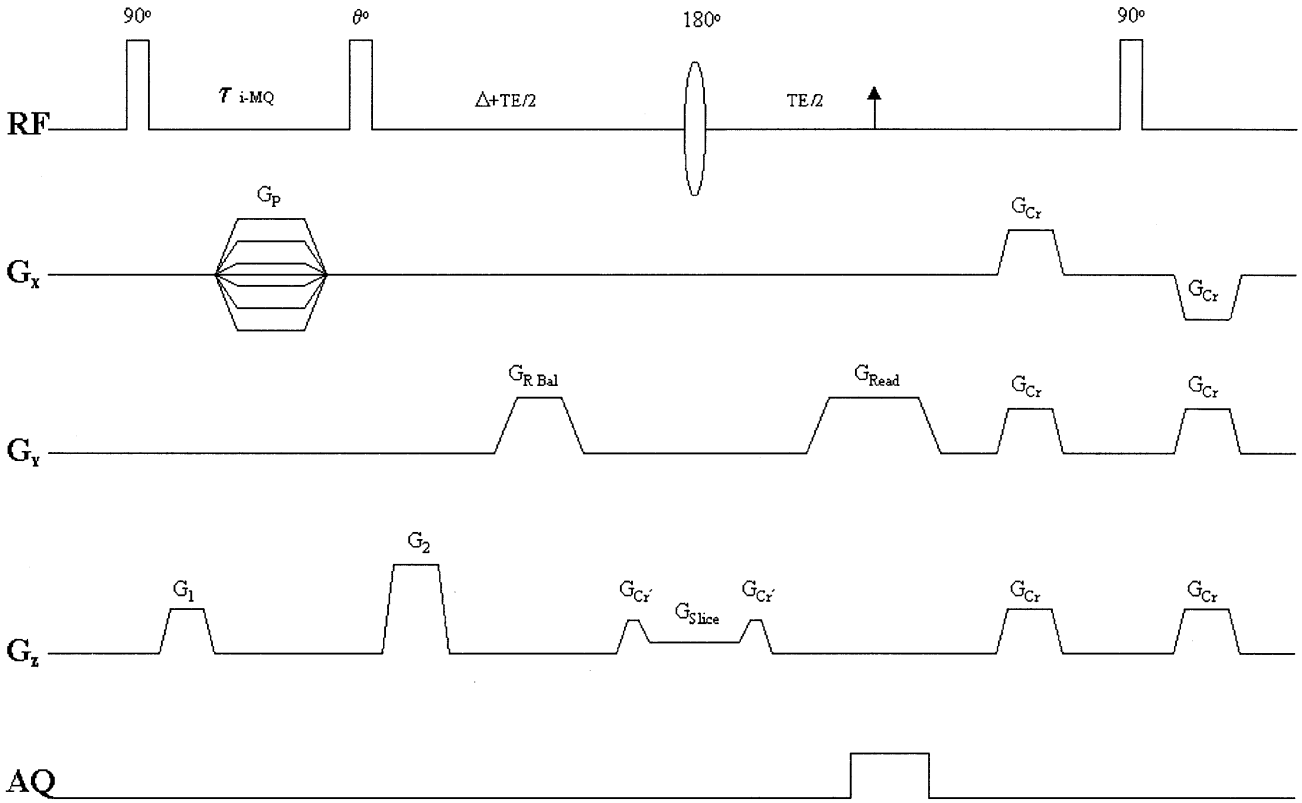

FIG. 1. Pulse sequence for 2D slice imaging using i-MQCs. G_1 and G_2 are coherence order selection gradients. (See text for details.) The arrow indicates the position of the echo.

and the echoes or antiechoes are frequency encoded by G_{Read}, the read gradient. The last 90° pulse along with the spoiler gradients G_{Cr} at the end of the sequence eliminates stimulated echoes (*2, 3*). We also employed the phase-cycling scheme of Minot *et al.* (*15*) to further improve the separation of the required coherence order.

Figure 2 shows the pulse sequence for 3D imaging with two phase encoding gradients G_{P} and $G_{\mathrm{P}'}$ applied during the evolution period of i-MQCs followed by frequency encoding of single quantum coherences. A hard 180° pulse along with crushers $G_{\mathrm{Cr}'}$ replaces the soft 180° pulse of the slice-selective version. Other symbols are as in the 2D sequence.

All the experiments reported here were implemented using a 500 MHz (11.7 T) Bruker AMX spectrometer running Paravision software for image acquisition. The i-DQC images shown were obtained with an actively shielded microimaging probehead employing a 10-mm birdcage RF coil maintained at 293 K. The experiments were conducted with a phantom consisting of one large tube with three inner tubes. The outer tube (i.d. ≈ 9 mm) and two inner tubes (i.d. ≈ 2.4 mm) were filled with water and one inner tube is empty. The reconversion flip angle θ° was 120°. The value of the pitch length is 156 μm for all the images. The Δ and TE were kept at 6 and 15 ms, respectively, for all the water phantom images. The images were thresholded individually and processed with the VoxelView software running on an SGI Indy work station. Unless stated otherwise, field-of-view (FOV) quoted in this Communication corresponds to phase and frequency encoding with SQCs.

Figure 3 shows 2-mm-thick slice images of the phantom obtained with a FOV of 2 × 2 cm. The view perpendicular to long axis of the tubes is displayed. The image shown in Fig. 3a was obtained with a conventional spin echo sequence. Figures 3b and 3c are i-DQC images obtained with the 2D sequence shown in Fig. 1. Figure 3b shows the i-DQC image obtained with phase encoding along *x* and read along the *y* direction. Figure 3c shows the i-DQC image obtained with phase encoding along *y* and read along *x* direction. The phase and read gradient values used in Fig. 3a, 3b, and 3c are identical. In Fig. 3b and 3c the cross sections appear elliptical with major-to-minor axis ratio of 2 : 1 and the major axis along the phase direction. Figure 3d was obtained with parameters identical to Fig. 3b, except that the phase-encode gradient increment was reduced by a factor of 2. The i-DQC images display slight B_1 inhomogeneity artifacts at the edges.

Figures 4a and 4b show two *x–y* slices extracted from 3D data sets. The FOV for the 3D images was 2 × 2 × 2 cm. Figure 4a was obtained with the sequence shown in Fig. 2. i-DQCs were phase encoded along two dimensions and the single quantum coherence was frequency encoded in the third dimension. Figure 4b displays the same slice obtained with a sequence

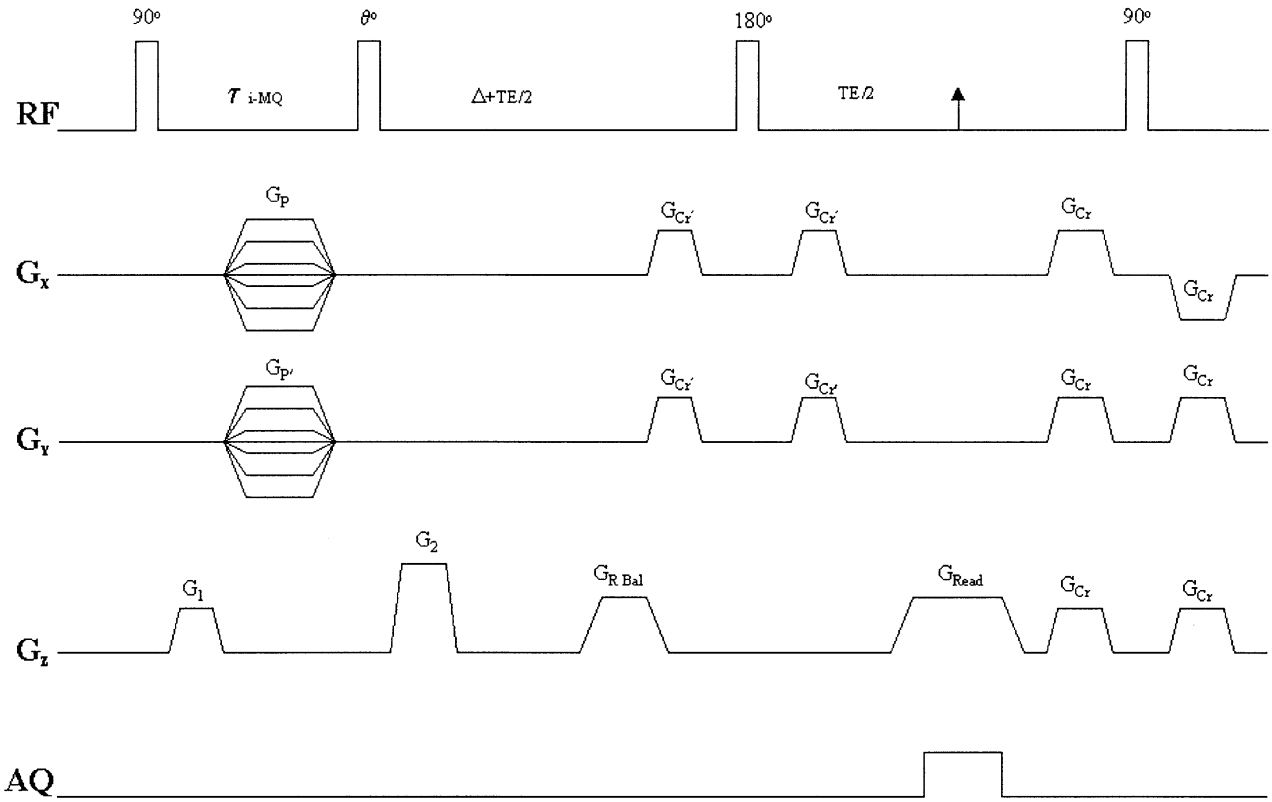

FIG. 2. Pulse sequence for 3D imaging of i-MQCs.

(not shown here) in which single quantum coherences converted from i-DQCs were phase and frequency encoded (*1–8*). The strengths of the phase encode and read gradients were kept the same for obtaining both the images. There is a distortion-free magnification of a factor of 2 for each phase encoding performed before conversion to single quantum coherence.

The integrity of the i-DQC signals was tested in several ways. Coherence gradients placed along the magic angle nulled the signal. Changing the coherence gradient from z to the x or y directions reduced the echo amplitude by half. The coherence selection was extremely sensitive to the ratio of the gradient pair G_1 and G_2, such that even a slight deviation from the correct ratio of $1:2$ resulted in a nulling of the signal. All these observations confirm that the signals generated were due to i-DQCs.

Interpretation of the effect of phase encoding in the multiple quantum versus the single quantum state is straightforward. Phase encoding the i-MQCs yields afield of view,

$$[\mathrm{FOV}]_{\mathrm{Phase(i\text{-}MQC)}} = \frac{1}{t \cdot n\gamma \Delta G}, \qquad [1]$$

where ΔG is the gradient increment which is the same for each phase step, t is the phase encode duration, and n is the coherence order. As expected, the standard expression for the FOV in the single quantum state is obtained when $n = 1$. Moreover, when an i-MQC of coherence order n is phase encoded with a gradient step size, ΔG, the "effective" step size becomes $n\Delta G$. Because the $\mathrm{FOV}_{\mathrm{Phase}}$ is inversely proportional to the step size it gets reduced by a factor n. This offers the advantage of employing reduced phase encode gradient amplitudes with i-MQCs and obtaining images with resolution equivalent to the normal single quantum image resolution.

The voxel size in 2D slice selective (i-MQC) image can be expressed as

$$V_{\mathrm{size}}(2\mathrm{D}) = \frac{[\mathrm{FOV}]_{\mathrm{Phase(i\text{-}MQC)}}}{nN_x} \cdot \frac{[\mathrm{FOV}]_{\mathrm{Read}}}{N_Y} \cdot \text{Slice thickness}, \qquad [2]$$

where n is the coherence order and N_x and N_y are the number of points along the phase and read directions. Since the FOV (SQC) in our case is 2×2 cm and N_x and N_y are 128, the in-plane resolution for the images shown in Figs. 3b and 3c are 78×156 and 156×78 μm along x and y directions, respectively. For images shown in Figs. 3a and 3d the in-plane resolution is 156×156 μm.

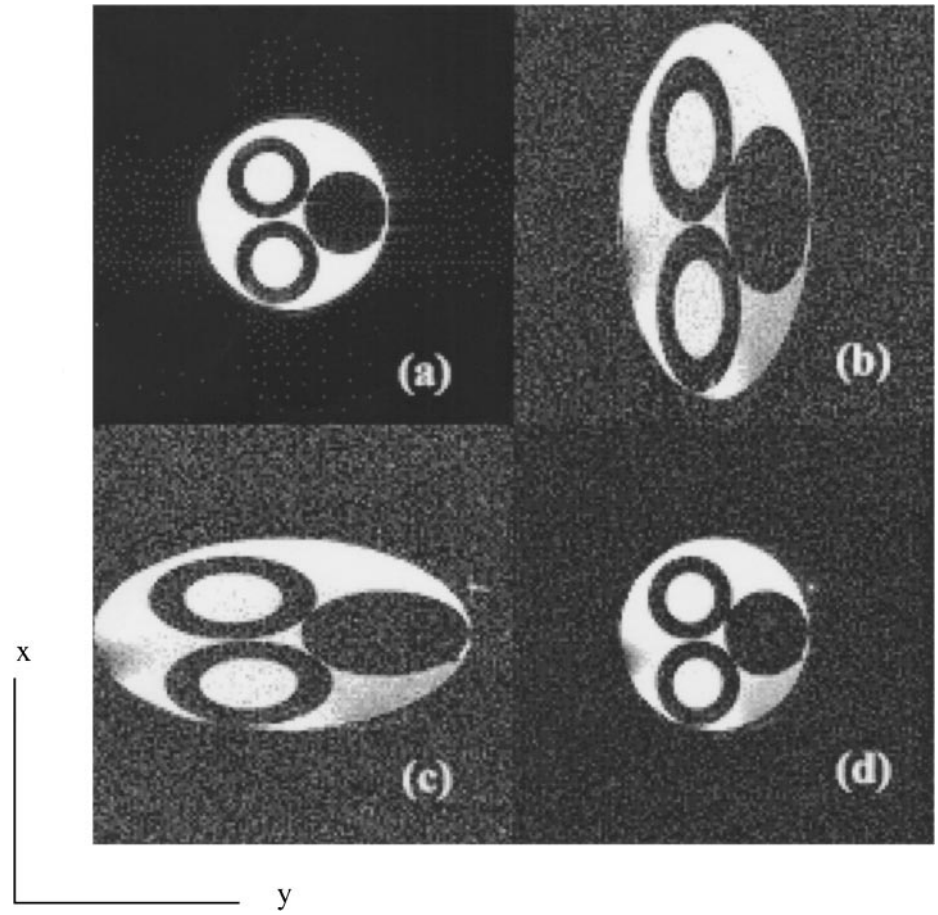

FIG. 3. Slice images: (a) spin echo; (b, c, d) i-DQC images obtained using the sequence shown in Fig. 1. (See text for details.) Slice thickness 2 mm. Matrix size 128 × 128, TR = 2 s, NS = 4, FOV (SQC) = 2 × 2 cm.

When multiple phase encode gradients are applied during the evolution of i-MQCs the voxel sizes get reduced by a factor of n for each phase encode direction. For example, in a 3D experiment where two phase encodes are applied during the i-MQC evolution period the voxel size is

$$V_{\text{size}}(3\text{D}) = \frac{1}{n^2}\frac{\text{FOV(i-MQC)}_{\text{phase}}}{N_x}\cdot\frac{\text{FOV(i-MQC)}_{\text{phase}}}{N_Y}\cdot\frac{\text{FOV(SQC)}_{\text{Read}}}{N_Z}, \quad [3]$$

where N_x, N_y, and N_z are the number of points along the two phase encodes and read directions and n is the order of the coherence. We can readily see that the voxel size is reduced by a factor of 4 by encoding both the phase directions with i-DQCs. The images shown in Fig. 4a and Fig. 4b correspond to an in-plane resolution of 156 ×156 and 312 × 312 μm , respectively. The resolution along the read direction is 156 μm. In both cases measurements of the signal-to-noise ratios for the i-DQC images correlate well with the voxel sizes derived in Eqs. [2] and [3].

Following Warren and colleagues (*10, 14*) the signal reconverted from i-MQC with coherence order n is given

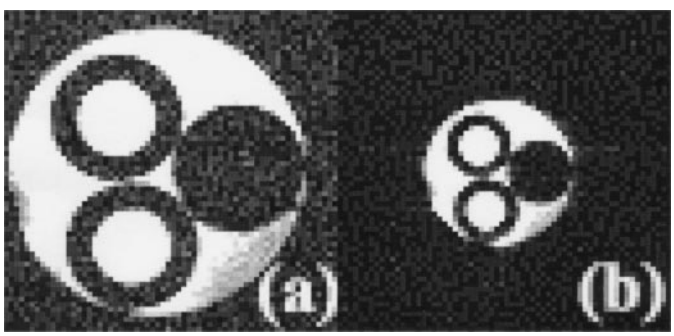

FIG. 4. 2D slices obtained from 3D data sets are shown. The 3D data size is 128 × 64 × 64. NS = 4, FOV (SQC) = 2 × 2 × 2 cm. The 2D slice dimension corresponds to 64 × 64 and TR = 1.5 s.

by

$$S(t_1, t_2) = i^{n-1} e^{i\omega_2 t_2} e^{-in\omega_1 t_1} M_0 \left(\frac{n\tau_d}{t_2 \Delta_s}\right) \times J_n \left(-\frac{t_2 \Delta_s}{\tau_d}\right) e^{-t_1/T_{2,\text{i-MQC}}} e^{-t_2/T_{2,\text{SQC}}}, \quad [4]$$

where ω_1, ω_2 are the frequencies of precession during the t_1 (n-quantum evolution) and t_2 (single quantum detection) periods with their respective transverse relaxation times. J_n is the nth order Bessel function; $\Delta_s = [3(\hat{s} \cdot \hat{z})^2 - 1]/2$ where $\hat{s}$ is the direction of the of the coherence gradients, and $\hat{z}$ is the static magnetic field direction, M_0 is the equilibrium magnetization per unit volume, γ is the gyromagnetic ratio, and μ_0 is the vacuum permeability. The dipolar demagnetizing time $\tau_d = 1/\gamma\mu_0 M_0$ amounts to approximately 76 ms in these experiments.

The expression for the signal acquired in i-DQC imaging with a reconversion flip angle $\theta = 120^\circ$ can be expressed as (*6, 16*)

$$S(t_1, t_2) = i M_0 e^{i\omega_2 t_2} e^{-i2\omega_1 t_1} \left(\frac{3\sqrt{3}}{4}\right) \left(\frac{2\tau_d}{t_2}\right) \times J_2 \left(-\frac{t_2}{\tau_d}\right) e^{-t_1/T_{2,\text{i-DQC}}} e^{-t_2/T_{2,\text{SQC}}}, \quad [5]$$

where $2\omega_1$ is the frequency of i-DQC during the evolution period and ω_2 is the frequency of the SQC converted from the i-DQC during the detection period. J_2 is the 2nd order Bessel function. The coherence gradients were applied along the z direction; hence $\Delta_s = 1$. Though the theory predicts a recovery of 36% of the initial magnetization for i-DQC images (*14*), our signal-to-noise measurements suggest that in practice a value up to 10% of initial magnetization is obtained. This might be attributed to T_2^* losses and diffusion. Contrast in an MR image is determined mainly due to the signal obtained in the absence of phase encode gradients, i.e., when $k = 0$ (*17, 18*). The k values corresponding to higher spatial frequencies generally contribute mainly to image resolution and definition. Contrast in the i-MQC images obtained using sequences described here is expected to be similar to that in sequences that phase encode SQCs filtered from i-MQCs. As emphasized by Warren and colleagues (*1, 3, 4, 14*), contrast can be optimized in these sequences by tuning the pitch length of the helix, thus varying the interaction distance between the spins which are correlated. The evolution period of the i-MQCs can also be varied to produce $T_{2,\text{i-MQC}}$ contrast as opposed to $T^*_{2,\text{i-MQC}}$ contrast by introducing a 180° pulse in the middle of the evolution period ($\tau_{\text{i-MQC}}$). This will refocus B_0 inhomogeneity and chemical shifts. By placing an additional pair of gradients symmetric to this 180° pulse i-MQC diffusion contrast can be produced. Different values of Δ and TE may be useful in biological samples and these parameters need to be optimized.

We have demonstrated that for a given gradient strength, phase encoding of the intermolecular double quantum coherence results in images with a factor of 2 increased resolution as compared to phase encoding of single quantum coherence reconverted from the intermolecular double quantum coherence. The images obtained by phase encoding the intermolecular double quantum coherence are free from contamination due to intermolecular zero quantum coherence except for the possibility at $k = 0$ line. This can be eliminated by appropriate phase cycling. The techniques outlined here can be easily extended to produce $T^*_{2,\text{i-MQC}}$, $T_{2,\text{i-MQC}}$, and i-MQC diffusion-weighted images. In general i-MQC signals are weaker than the SQCs employed in conventional imaging. However the contrast produced in i-MQC images makes these sequences attractive.

ACKNOWLEDGMENTS

This work was funded in part by the Human Brain Project (DA08944) with contributions from the National Institute on Drug Abuse and the National Institute of Mental Health, and the National Center for Research Resources (RR13625).

REFERENCES

1. W. Richter, S. Lee, W. S. Warren, and Q. He, Imaging with intermolecular multiple-quantum coherences in solution nuclear magnetic resonance, *Science* **267,** 654–657 (1995).
2. S. Mori, R. E. Hurd, and P. C. M. van Zijl, Imaging of shifted stimulated echoes and multiple spin echoes, *Magn. Reson. Med.* **37,** 336–340 (1997).
3. W. S. Warren, S. Ahn, M. Mescher, M. Garwood, K. Ugurbil, W. Richter, R. R. Rizi, J. Hopkins, and J. S. Leigh, MR imaging contrast based on intermolecular zero quantum coherences, *Science* **281,** 247–251 (1998).
4. R. R. Rizi, S. Ahn, D. C. Alsop, S. Garrett-Roe, M. Mescher, W. Richter, M. D. Schnall, J. S. Leigh, and W. S. Warren, Intermolecular zero-quantum coherence imaging of the human brain, *Magn. Reson. Med.* **43,** 627–632 (2000).
5. W. Richter, M. Richter, W. S. Warren, H. Merkle, P. Andersen, G. Adriany, and K. Ugurbil, Functional magnetic resonance imaging with intermolecular multiple-quantum coherences, *Magn. Reson. Imaging* **18,** 489–494 (2000).
6. J. Zhong, Z. Chen, and E. Kwok, In vivo intermolecular double-quantum imaging on a clinical 1.5 T MR scanner, *Magn. Reson. Med.* **43,** 335–341 (2000).
7. J. Zhong, Z. Chen, and E. Kwok, New image contrast mechanisms in intermolecular double-quntum coherence human MR imaging, *J. Magn. Reson. Imaging* **12,** 311–320 (2000).
8. P. T. Narasimhan, S. Sendhil Velan, and R. E. Jacobs, 3D-MR microscopy of the mouse brain with intermolecular zero and double quantum coherences at 11.7 T, Proceedings of the International Society of Magnetic Resonance in Medicine, Denver, p. 2074, (2000).
9. W. S. Warren, W. Richter, A. H. Andreotti, and B. T. Farmer II, Generation of impossible cross-peaks between bulk water and biomolecules in solution NMR, *Science* **262,** 2005–2009 (1993).
10. S. Vathyam, S. Lee, and W. S. Warren, Homogeneous NMR spectra in inhomogeneous fields, *Science* **272,** 92–96 (1996).
11. N. M. Szeverenyi and E. M. Haacke, Applications of multiple quantum coherence to MR imaging, *J. Comput. Assist. Tomogr.* **10,** 484–489 (1986).
12. N. Chandrakumar and S. Sendhil Velan, Multiple-quantum-single-quantum NMR images, *J. Magn. Reson. A* **104,** 115–118 (1993).
13. J.-M. Bohlen, M. Izquierdo, and M. Décorps, Simultaneous observation of single and multiple-quantum coherence images by gradient proportional phase incrementation (GPPI), *J. Magn. Reson. A* **110,** 106–108 (1994).

14. S. Lee, W. Richter, S. Vathyam, and W. S. Warren, Quantum treatment of the effects of dipole-dipole interactions in liquid nuclear magnetic resonance, *J. Chem. Phys.* **105,** 874–900 (1996).

15. E. D. Minot, P. T. Callaghan, and N. Kaplan, Multiple echoes, multiple quantum coherence, and the dipolar field: Demonstrating the significance of higher order terms in the equilibrium density matrix, *J. Magn. Reson.* **140,** 200–205 (1999).

16. R. Bowtell, R. M. Bowley, and P. Glover, Multiple spin echoes in liquids in a high magnetic field, *J. Magn. Reson.* **88,** 643–651 (1990).

17. Michael L. Wood, Fourier imaging, *in* "Magnetic Resonance Imaging" (D. D. Stark and W. G. Bradley, Eds.), Vol. 1, pp. 21–66, Mosby-Yearbook, St. Louis (1992).

18. F. W. Wehrli, "Fast-Scan Magnetic Resonance: Principles and Applications," Chap. 2, Raven Press, New York (1990).